



Optimizing Airborne Emission Rate Retrievals with Sub-Hectometre Resolution Numerical Modelling

Sepehr Fathi^{1,2}, Mark Gordon³, Jingliang Hao³

- ¹ Air Quality Research Division, Environment and Climate Change Canada, 4905 Dufferin Street, Toronto, ON M3H 5T4, Canada
- ² Formerly at Physics and Astronomy Department, York University, 4700 Keele Street, Toronto, ON M3J 1P3, Canada
- ³ Department of Earth and Space Science and Engineering, York University, 4700 Keele Street, Toronto, ON M3J 1P3, Canada

Correspondence to: Mark Gordon (mgordon@yorku.ca)

Abstract. A comprehensive model-based study is designed to provide optimal flight paths for airborne top-down emission rate retrieval methodologies. The meteorology and plume dispersion were modelled using the Weather Research and Forecasting (WRF) modelling platform with the Advanced Research WRF (ARW) dynamical core at 50-m resolution. Multiple flight path designs and parameters were investigated to determine emission rate retrieval accuracy as a function of downwind distance and transect spacing, which are ultimately related to flight time and cost. Three unique source types (multiple smokestack plumes, small area sources, and a large area source) were investigated for 4 summer afternoon flight cases over 2 days. The results demonstrate that emissions estimate uncertainty is primarily due to storage and release. The average advective flux estimates are within 12% of the known emissions for downwind distance of D ≥ 4 km. Variability between flights decreases with D. For stack sources the variability near D = 10 km is approximately half that at D = 4 km. For small area sources, there is less reduction with D, and for the large area source, variability reaches a minimum at D = 8 km. For stack sources, transect spacing is optimized at 100 m, while for area sources, a spacing of 50 m reduces uncertainty. Error due to extrapolation below the lowest flight path is less than 20% for stack sources and less than 30% for area sources for non-dimensionalized downwind distance of D' ≥ 3. Results demonstrate the need for surface sampling coincident with the flights to reduce extrapolation error, and the use of modeling with reanalysis data to account for storage and release effects.

25 1 Introduction

During airborne field studies for top-down retrieval of source emission rates, the environmental fields (meteorology and pollutant concentrations) are sampled around and/or downwind of emission sources. Typically, the aircraft flies in a repeating pattern that either encloses the source area (e.g., Peischl et al., 2010; Kalthoff, 2002; Gordon et al., 2015; Kim et al., 2025), or that captures the extent of a downwind plume (e.g. Cambaliza et al., 2014). The time and spatial resolutions of such measurements are determined by the sampling frequency and range of the measuring instruments, the speed of the



35

40



sampling platform, the sampling path and geographical locations (Gordon et al., 2015; Conley et al., 2017). The sparse spatial measurements that are made over time are processed and analyzed according to various assumptions regarding how representative they are of the mean and real-time environmental conditions (e.g., wind field, emissions: Alfieri et al., 2010). The post-processed data are then used for estimating emission rates from sources of pollution (Ryoo et al., 2019; Karion et al., 2015; Gordon et al., 2015).

Regardless of the measurement approach, the spatial heterogeneity and temporal variability of meteorology and concentration fields can result in large uncertainties in top-down estimates. Previous studies have attributed large uncertainties (20% to 40%) to the gap of information (spatial and temporal) in the sampled data (e.g., Angevine et al., 2020). For instance, airborne measurements are commonly made at elevations above 150 m agl for safety considerations. Gordon et al. (2015) identified the unsampled region below the lowest flight level as a large source of uncertainty in mass-balance analysis (e.g., up to 26% for CH₄ plumes). The gap of information in the sampled data, due to limitations on spatio-temporal resolution and range of the sampling method, can be partially filled by combining data from different measurement platforms. For instance, airborne samplings (aircraft, UAV) can be complimented by ground-based measurements (Brus et al., 2021b; Bell et al., 2021; Islam et al., 2021). Fixed location in-situ measurement techniques of meteorology and tracer concentrations include tower measurements at heights of up to 350 m agl (Heintzenberg et al., 2011; Andreae et al., 2015), and radiosonde (tethered/balloon) measurements include heights up to 2 km agl (Nygård et al., 2017; Nambiar et al., 2020). Ground-based remote-sensing can also be conducted from mobile surface land vehicles (de Boer et al., 2021; Davis et al., 2019), generating column measurements at higher spatial (horizontal) resolution. Remote-sensing datasets can be analyzed in conjunction with airborne measurements for both validation (Davis et al., 2020) and as complementary information (Krings et al., 2018; Brus et al., 2021a) in air quality studies. In a study based on the same model output used in this study, Fathi (2022) suggests augmenting airborne in-situ measurements with aircraft-based remote sensing (lidar) towards improving aircraft mass-balance retrievals.

Dispersion models have also been used to infer emissions from aircraft measurements, as alternative to the more common mass-balance approach. For example, Karion et al. (2019) used an inverse approach comparing different dispersion models (HYSPLIT, STILT, LPDM, FLEXPART) that optimizes emission rates to best fit observation. However, there was significant range in the predicted emission rate depending on the model used. Simpler, Gaussian footprint models can also be used to similar effect (Kim et al., 2025). These techniques offer the advantage of being able to estimate emission rates from multiple sources when the plumes overlap (e.g. Kostinek et al., 2021; Raznjevic et al, 2022). This is more difficult to do with the mass-balance method and requires induvial plumes to be well defined and separate (e.g. Baray et al., 2018).

To better understand the mass-balance method and to quantify uncertainties, models can also be used to optimize the mass-balance measurement technique. Virtual aircraft can fly through model output fields, where emissions are known and the relative contributions of advection, turbulence, and flux below the lowest flight path can be determined. This also allows different flight configurations to be compared and optimized to increase emission measurement accuracy as a function of flight time (cost). Panitz et al. (2002) were the first (to our knowledge) to use model output to evaluate the aircraft mass-





balance method. They used the KAMM/DRAIS model system to evaluate box flight measurements described in Kalthoff et al. (2002). They determined advective fluxes were 85% of NO emissions and 95% of CO emissions, suggesting that total emissions estimated based on downwind advective flux measurements, could be underestimated by up to 15% (for NO) or 5% (for CO) by neglecting other terms in the mass-balance equation. Conley et al. (2017) appear to be the first to fly a spiral (or cylinder) flight pattern, which was proposed in Gordon et al. (2015) and used in Han et al. (2024). Conley et al. (2017) ran LES simulations to optimize the spiral radius and the number of passes. It is demonstrated that a minimum non-dimensional radius can be determined, as

$$R' = \frac{Rw_*}{Uz_i},\tag{1}$$

where R is the actual radius, w_* convective velocity, U mean wind speed, and z_i boundary-layer height. A value of R' > 0.45 resulted in nearly constant concentration below the lowest flight path (150 m), which reduces the uncertainty due to extrapolation of these unknown values. Using order-of-magnitude estimates of $w_* = 1$ m/s, $z_i = 1000$ m, and U = 10 m/s, gives R = 4.5 km (as an example). Conley et al. (2017) also test the number of laps around the source required to reach convergence over multiple tests and find that 15 or more laps (at a normalized radius of R' = 0.25) are required to repeatedly produce the most accurate results (which is an accuracy of near 85% in this case). However, a real-life controlled release experiment suggests that as many as 25 laps are required to reach comparable accuracy.

This study aims to optimize flights to determine emission rates from large emitting stacks in industrial complexes such as the Canadian oil sands (Liggio et al., 2019; Li et al., 2017). These kinds of operations typically include stack emissions, dust and vehicle exhaust from roadways that connect different operations, surface sources of pollution that span over a large area such as surface mine excavation sites, and larger area sources such as tailings ponds (Baray et al., 2018; Davis et al., 2020).

Various emission scenarios (e.g., point, area sources) and tracer dispersion and transport under different meteorological conditions were simulated using a high-resolution WRF model described in Fathi et al., 2023. The output data from this high-resolution (with LES parameterization) WRF model is assessed here as a proxy for real-world environmental fields (virtual sampling). The range of spatial and temporal variability in fields sampled by a mobile platform for top-down retrievals can impact the accuracy of the estimates. For example, spatio-temporal variability in sampled fields is dependent on the downwind distance and hence investigating the optimized sampling distance using model data (following Conley et al., 2017) is desirable and can provide valuable advice in terms of observational flight planning and data processing. By studying the output fields from several different WRF simulation scenarios, we investigate the impact of different sampling strategies on the accuracy of top-down estimates and provide operational recommendations for general and specific cases.





.2 Methods

95

100

105

110

115

125

2.1 Case Studies and Locations

This analysis uses WRF output data described in Fathi et al. (2023). The model is run at a resolution of $\Delta x = 50$ m, $\Delta z \approx 12$ m, and $\Delta t \leq 1$ s, which is often referred to as "super-resolution" (Wu et al., 2021; Onishi et al., 2019; and Watson et al., 2020). The WRF model output data span a geographical location over the northwest portion of Athabasca oil sands region, Alberta, Canada. Although three different cases were simulated in Fathi et al. (2023), we focus here on Case 1 on Aug 20 (all dates in 2013) and Case 3 on Sep 2. Case 2 on Aug 26 was a stagnant, low-wind speed case with high vertical wind shear. For this case, the vertical motion of the plume in the presence of strong wind shear resulted in plume recirculation causing significant storage within the control volume during the flight time. Hence. Case 2 was not considered suitable for the massbalance technique (see also Fathi et al., 2021 for more discussion of this effect). The dates of Case 1 and 3 coincide with aircraft emission retrieval flights over the CNRL facility in the northwest area of the oil sands region, during the 2013 JOSM (Joint Canada-Alberta Implementation Plan on Oil Sands Monitoring) field campaign (JOSM, 2013) and they are the two flights described in detail in Gordon et al. (2015). Both cases (summer, afternoon flight times) demonstrate thermally and dynamically unstable conditions in both the measurements (Gordon et al., 2015) and model output (Fathi et al., 2023). In this study, we simulate aircraft measurements around and downwind of the CNRL facility using the model output data as proxy for real-world environmental fields (virtual sampling). To achieve this, we extract data from the model 4D fields for time periods and along flight paths similar to those conducted during airborne field campaigns. The super-resolution of our model-generated atmospheric fields allow us to sample data at temporal and spatial scales of airborne measurements without the need for interpolation of model generated fields. The model simulations are also capable of resolving atmospheric dynamical processes (turbulence) at airborne sampling scales and therefore provide us with ample information for investigating the impact of spatio-temporal variability in sampled fields on the accuracy of top-down estimates. We analyze the model-generated data as if they were observational data to retrieve emission rates from various sources within the facility. We then evaluate these estimates against the known modelling conditions (i.e. emission rates, meteorology) to optimize the flight parameters.

2.2 Model Description

Model details are discussed in Fathi et al. (2023) and are summarized here. The Weather Research and Forecasting model (WRF, version 3.9) was used with the ARW dynamical core. In this analysis, we use the velocity components (u, v, w), meteorological parameters (temperature, T, pressure, p, and moisture, χ), and 11 tracer scalars, corresponding to different point, line, and area emission sources (described below). ARW solves for advection of momentum, scalars, and geopotential in flux form (the governing equations).

Five nested grid domains are used in both the horizontal and vertical, with increasing horizontal resolution from ~31 km to 50 m, and vertical resolution of 11.2 m (for the lowest 40 grid levels in the finest domain), and a time step of 0.16 s (in the



130

135

140

145

150



finest domain). The coarsest domain was driven with North American Regional Reanalysis (NARR) GRIB (GRIdded Binary) data (at 3 h intervals) from NOAA (National Oceanic and Atmospheric Administration) archives. Our WRF-ARW model configuration conserves mass within 1–5% and successfully resolves turbulent eddies at aircraft-observed scales by leveraging the full suite of large-eddy simulation (LES) options. For details of the super-resolution modelling setup, see Fathi et al. (2023).

The 11 tracer emission locations comprise a combination of real and hypothetical sources, which include 7 elevated (stack) sources, two small area surface sources (surface mines), a large area source (tailings pond), and a multi-section line source (heavy-hauler roadway). 7 of the 11 source locations are shown in Figure 1. A hypothetical super-elevated stack with a height of 483 m (CNRL0), 2 hypothetical upwind 102 m tall stacks (CNRLw and CNRLs), and a highway (HWY) were used in Fathi et al. (2023) for model testing but these sources are not used in this analysis. The existing stacks (CNRL1-4) range in height from 30 to 114 m in height. The large area source (POND) is approximately 50 km², and the small area sources (MINE1 and MINE2) are 550 m × 550 m and 350 m × 550 m, respectively. Each source emits a known amount, E_S , which can be compared to the emissions determined from the TERRA mass-balance method, E_{Total} , discussed in Section 2.3. Emissions from each source are independent in the model and are treated separately. Here we evaluate three emissions scenarios: stacks (the sum of CNRL1, 2, 3, and 4), small area sources (the sum of MINE1 and MINE2), and the large area source (POND).

Meteorological and tracer values were output from the finest domain every 1-second over the area shown in Figure 1 (also extending south of what is shown in the figure to 57.15 N). Model runs start at 09:00 local time (15:00 UTC). The Aug 20 run stops at 18:47 UTC and the Sep 2 run stops at 18:09 UTC. As discussed in Fathi et al. (2023), meteorological fields converge in under 1 hour of simulation. All analysis discussed herein starts after 16:20 UTC (80 minutes after startup) to allow more than enough model spin-up time for the meteorological fields to converge over the modelling domain and ensure that all the plumes have reached the edge of the model domain.

2.3 Mass-Balance Calculation

Airborne top-down emission rate retrievals are usually accomplished by flying at a distance downwind of the emission source and at several altitude levels. Although flights that are far enough downwind of a source (or over a large homogenous surface source) can assume a well mixed boundary layer and fly at a single altitude (e.g. Turnbull et al., 2009; Karion et al., 2013; Hiller et al., 2014), we restrict our analysis here to relatively short flights (~10's of kms) where the plume is not uniformly mixed and flights at multiple heights are required to characterize the plume (Fig. 1).



160

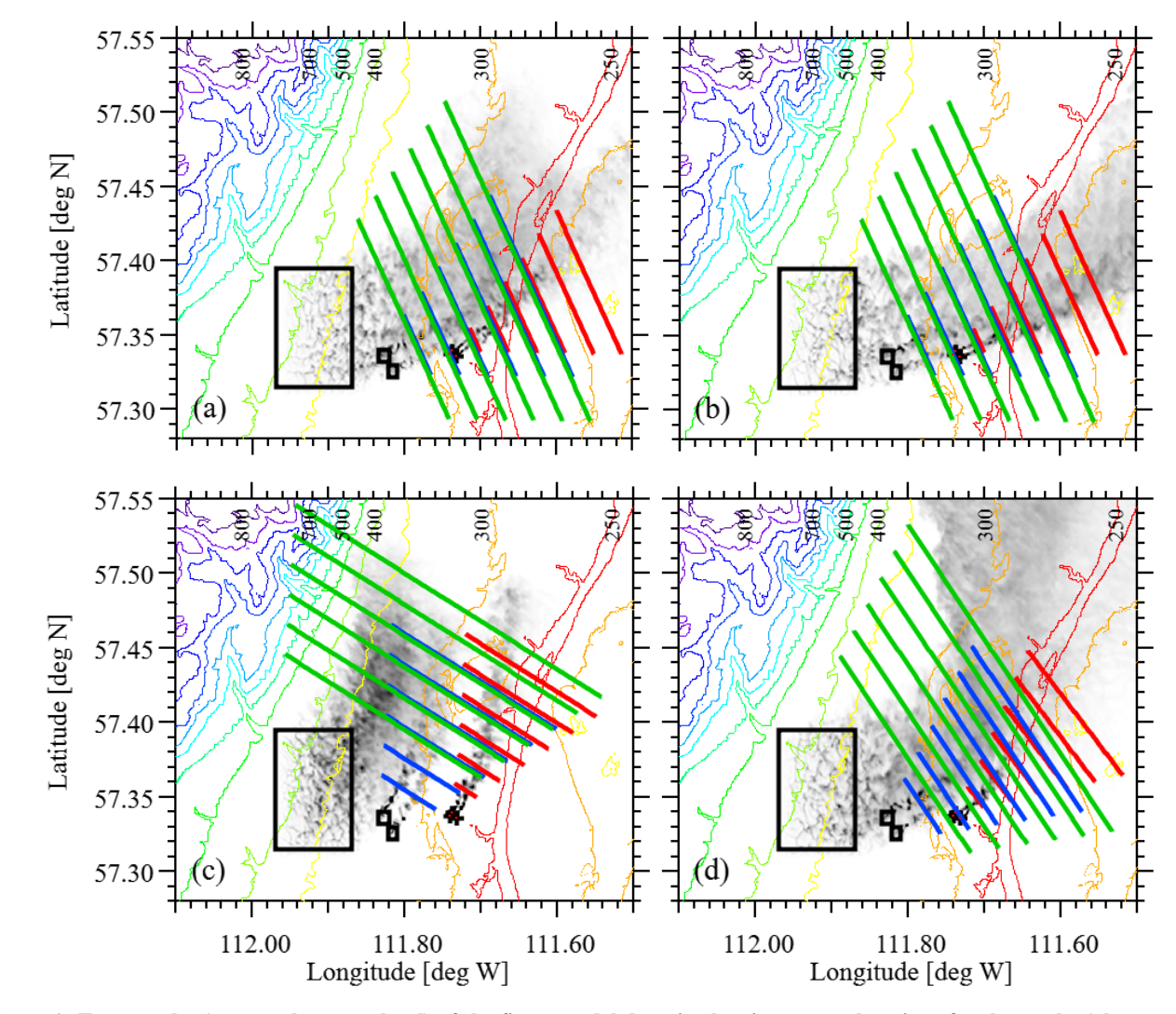


Figure 1: Topography (meters above sea-level) of the finest model domain showing source locations for the stacks (plus symbols), two small area sources, and the large area source (black rectangles). All stacks are combined as stack sources, and the two small areas are combined as the small area sources. Plumes (integrated total concentrations with arbitrary scales) are shown as instantaneous snapshots at Aug 20 16:20 (a) and 17:20 (b), and Sep 2 16:20 (c) and 17:10 (d). Flight paths are shown for each of the three source locations at downwind distances of D = 2, 4, 6, 8, 10, and 12 km for the stack sources (red lines), the small area sources (blue lines), and the large area source (green lines). The model domain extends to 57.15 N, but only north of 57.30 N is shown here.

165 Following the TERRA algorithm outlined in Gordon et al. (2015) the emission rate within a control volume can be calculated as

$$E_{Total} = E_H + E_{HT} + E_V + E_{VT} + E_{VD} - E_M - E_X + S, \tag{2}$$



170

175

185



where E_{Total} is the total emissions rate integrated over all activities within the facility, E_H is the horizontal advective flux through the box walls, E_{V} is the advective flux through the box top, E_{V} is the turbulent flux through the box top, E_{V} is the deposition to the surface, E_{M} is the increase in mass within the volume due to a change in air density, and E_{X} is the increase in mass due to chemical changes of the compound within the box volume. As demonstrated in Fathi et al. (2021), a storage term (S) must be included to account for emissions trapped within the control volume or released from the control volume after a previous build-up. Fathi et al. (2021) demonstrate that storage/release is related to non-steady state wind conditions, changes in stability, vertical wind shear, and upwind emissions (for enclosed flight patterns).

As past studies have shown (Kalthoff et al., 2002; Gordon et al., 2015), the most significant term in Equation 2 is the horizontal advective flux. This is calculated by first creating a 2-dimensional screen from the flight measurements (using some form of interpolation), with horizontal dimension s, and vertical dimension s, transformed from the 4-dimensional (x, y, z, t) measurements The advective flux is then calculated as

$$180 \quad E_H = \iint C U_\perp ds \, dz, \tag{3}$$

where s is the distance along the flight path, z is the height from the ground, C is the species concentration at each screen location (s, z), and U_{\perp} is the wind speed perpendicular to the screen at that location, calculated as $U_{\perp} = \vec{U} \cdot \hat{n}$, where \hat{n} is the unit vector (horizontal) normal to the flight path, s (positive outward).

The simplest and lowest cost approach (i.e. least flight time) is to ignore the control volume and fly in a single screen downwind of the plume (e.g. Mays et al., 2009; Cambaliza et al., 2014). A background concentration must be calculated either from an upwind pass or from the plume edges. The terms E_V , E_{VT} , and E_M in Equation 2 must be ignored, although E_{HT} , E_{VD} , and E_X can be estimated if the plume source location is known. When multiple downwind screens are used, this method can be used to estimate deposition (E_{VD}) in the area between the screens (e.g. Liggo et al., 2019; Hayden et al., 2021).

To assess the upwind fluxes and to better estimate all the terms in Equation 2, the plane can fly in a repeating closed circuit at different heights to trace a 3-dimensional prism. In actual flights at this location (Gordon et al., 2015; Liggio et al., 2019; He et al., 2024), rectangular "box" shapes (or a 5-sided near-rectangle with a cut corner) were flown with sides aligned with compass directions (and facility roads and layouts). In this study, we focus only on screen flights and then extrapolate these results to estimate the uncertainties in enclosed flight patterns. To calculate the emission rate for an enclosed cylinder or box flight, the perpendicular wind speed (U_1) in Equation 2 must take into account the changing flight path direction.

Interpolation of the 2D screens is done with the kriging method, which is standard for multiple-path screen flights (e.g. Cambaliza et al., 2014, Gordon et al., 2015, Ryoo et al., 2019, Kim et al., 2025). The kriging algorithm used here (Wavemetrics) fits a spherical function to the variogram to determine the appropriate range value. Here, the screens are interpolated to a resolution of $40 \text{ m} \times 20 \text{ m}$ (s and z respectively).



210

215

220

225

230



Although various extrapolation methods are available to fill the values between the lowest flight path and the ground (Gordon et al., 2015), for simplicity we assume a constant value between the ground and lower flight path equal to the concentration at the height of the lowest flight path, representing a well-mixed concentration in the boundary-layer. As discussed above, Conley et al. (2017) determine the optimized flight radius (R' in Eq. 1) for a cylindrical pattern as the minimum downwind distance at which the concentration is uniformly mixed (constant) below the lower flight path. Here, we use known model output to optimize the flight distance based on downwind distance of the screen and we investigate the accuracy of this extrapolation method, and whether other extrapolation methods (e.g. linear to zero at the surface, half-Gaussian) would improve emission estimation.

The second largest term in Equation 2 is typically the storage term, although it is never (to the authors' knowledge) accounted for in mass-balance estimation. Conley et al. (2017) include the flux divergence (analogous to storage/release) in their derivation but demonstrate that it is at least an order of magnitude less than the gradient term (as estimated by the advective flux) under ideal conditions. Reproducing actually flown box-flight patterns (as part of the JOSM campaign) on the same days simulated in this study (Aug 20 and Sep 2), and sampling SO₂ (primarily from stack sources), Fathi et al. (2021) found that S/E_S was -3% for the Aug 20 flights and -29% for the Sep 2 flights (negative storage is termed release and represents net loss from the control volume enclosed by the box flight after a previous build-up). Using the same model setup discussed in this paper, Fathi et al. (2023) determined the storage term for a box flight enclosing all the sources with an east wall 5 km downwind of the stack locations. The normalized storage term, S/E_S , for the emissions released from the 4 existing stacks (CNRL1-4), the surface mines (MINE), and the tailings pond (POND), ranged from -10.9% to -2.9% for Aug 20 and -27.5% to 15.4% for Sep 2. Hence, storage can be significant even when winds appear to be steady state, and optimization of flight parameters must consider how to reduce this uncertainty.

2.4 Flight Parameters

Screen and circuit emission retrieval flights can be flown with a variety of aircraft sizes, including UAVs (Han et al., 2024; Yong et al., 2024), small aircraft such as Cesna (Krings et al. 2018; Fiehn et al., 2020; Conley et al., 2017), or larger aircraft, such as Convair (Gordon et al., 2015; Liggio et al., 2019; Kim et al., 2025). UAV speeds range from 2 to 18 m/s, small aircraft typically fly between 40 and 75 m/s, while larger aircraft flight near 100 m/s and up to 150 m/s. Sampling rates can vary from 0.5 to 2 Hz, depending on the instrument used, resulting in a wide variety of horizontal sampling scales. In this study, we use a sample distance of 100 m (100 m/s at 1 Hz) to fly through the model space, following the scale of actual studies done at this location (e.g. Gordon et al., 2015; Liggio et al., 2019). These results can potentially be scaled to smaller aircraft sizes (or UAVs).

The lowest flight path is taken as 150 m agl (above ground level), following standard restrictions (e.g. Gordon et al., 2015; Conley et al., 2017). We assume an upward flight path, starting at 150 m agl and moving upward to a new height after each circuit or screen transect. During an actual field campaign, the concentrations can be monitored in real time, and sampling can be stopped after the last transect samples only background concentration (to avoid wasted flight time). To mimic this in



235

240

245

250

255

260

265



model space, the aircraft flies through the model up to a height of 800 m (well above all tracer emissions), but upper transects above the first background-level transect are removed from the analysis and not counted towards the total flight time.

Multiple screens are flown at distances D=2, 4, 6, 8, 10, and 12 km downwind of the smokestack location or edge of the line or area source. To account for plume spread, the screen length is determined as $L=L_0+2D\sin\varphi$, where L_0 is the width of the line or area source perpendicular to the wind ($L_0=0$ for smokestack sources), and φ accounts for the spread of the plume with downwind distance. Based on visual inspection of the plume spread in the model, we choose $\varphi=30^\circ$ to ensure the entire plume is captured under varying wind conditions. For smokestacks, this simplifies to L=D. Figure 1 shows the resulting screen lengths. In actual flights, the screen length would likely be determined in real time by observing concentrations while flying through the plume.

For these screens, the vertical transect spacing (i.e. the height between each subsequent pass along the screen length) is T = 100 m, to match the horizontal spacing. Once the screen distance is optimized, the transect vertical spacing is optimized for that distance by analyzing flights with T values of 50, 100, 150, and 200 m. At the end of each transect, 1 minute is added to turn the aircraft around and elevate to the next transect level but no measurements are taken during these maneuvers.

For each value of D or T, 10 flights are flown to provide a statistical evaluation of the variability and uncertainty in the emissions estimates. Assuming the values are normally distributed, we are 95% confident that the calculated mean is within $\pm 0.62\sigma$ (S.E. = $1.96\sigma/\sqrt{n}$, where σ is the standard deviation of the n=10 measurements). Based on our estimation of σ we can estimate the uncertainty that would be associated with a "real" single flight (S.E. = $1.96\sigma/\sqrt{n}$, with n=1). When comparing variability, it is noted that, for 10 samples, we are 95% confident that our estimate of σ is within 45% of the true value.

Each flight begins at the most NW location at a height of 150 m agl. There are two sets of flights on each of the two days for each of the three sources. The first set starts at 16:20 UTC. The second set starts at 17:20 UTC on Aug 20 and 17:10 UTC on Sept 2. For each set, each of the 10 flights starts 1 minute later than the previous flight (e.g. start times = 16:20, 16:21... 16:29). To simulate turbulent fluctuations in the flight, at each 1-s timestep of the flight, the horizontal aircraft speed is randomly offset by a Gaussian random number with a standard deviation of 3 m/s and the vertical position is offset by a Gaussian random number with a standard deviation of 1 m. Although these offsets are less than the model grid sizes, they are cumulative in effect during the flight, and they change the kriging results of the interpolated screen relative to an even spacing with no offsets. The temporal and spatial offsets ensures that each of the 10 flights (for each D and T value) is distinct but generally sampling the same meteorological and emission conditions. Although Conley et al. (2017) normalize R (to give R' in Equation 1), here we present D as dimensional (km) lengths and investigate non-dimensionalization further in Section 3.4.

For comparison, we also output the full model screen at one instant in time. In this case, the concentration at all grid cells along the screen (between the surface and 800 m agl) is output. This calculates all the tracer mass passing through the screen



270

275

280

285

290

295



at a given time, removing the effect of spatially sampling a temporally changing environment. By sampling at the grid square spacing from the surface (i.e. no lowest flight path height restriction), this removes the uncertainty associated with both kriging interpolation and extrapolation below the lowest flight path. These screens are flown at downwind distances of D = 2, 6, and 10 km. To investigate the variability of the E_H value estimated by this method (primarily associated with the storage term, S), 10 flights are flown at each distance, starting at 16:20 UTC with each subsequent screen 1 minute later. We refer to these flights and the calculated emission rate values as "instantaneous".

2.5 Meteorological Conditions

Figure 2 show the temperature (T) and winds (U,V) from the model at a height of 150 m above ground level for the two dates at three locations: the stacks, the centre of the small area sources, and the centre of the large area source. The flight durations are also shown for comparison (straight lines on the T-axis) for the two sets of flights on each date. The instantaneous flights (the shortest lines) span 9 minutes (e.g. 16:20, 16:21... 16:29). The longest screens downwind of the stack sources (at D = 12 km) span approximately 27 minutes, including 18 minutes of flight time plus 9 minutes since each of the 10 flights is offset by 1 minute each. Similarly, the longest small area and large area flight span 32 and 49 minutes, respectively. Screen flights closer to the source are always shorter in duration since the screens lengths are shorter, the plume tends to be lower to the ground and less transects are required to capture the entire plume.

The friction velocity (u_*) and the bulk Richardson number (Ri) demonstrate the turbulence and the and stability conditions, respectively. The largest bulk Richardson number (shown in Fig. 2 as a negative value on a log scale) is Ri = -0.49, which demonstrates that the conditions are always unstable during these model runs (using a criteria of 0.25 > Ri > -0.25 for neutral conditions). Temperature rises consistently during both afternoons, rising approximately 3°C on Aug 20 and 4°C on Sept 2. Although these two afternoons were chosen for their steady-state conditions, the winds can vary considerably over time and between different locations, demonstrating potential for storage and release during the flights.

2.6 Enclosed Flights

Although the single-screen flight is the most efficient way sample emissions since it captures the greatest downwind area without expending flight time flying upwind of the emission source, there are sometimes situations where an enclosed flight path (such as a cylinder or box flight) is necessary. For a small downwind distance, it could be more economical to continue in a circle (or spiral) pattern around the source, eliminated the need for the tight turning circle at the end of each screen transect. Or the aircraft could be equipped to measure multiple pollutants (potentially from multiple sources), and a single, large, enclosed flight path can capture a volume containing all the emission sources better than a single screen much further downwind. Or there may be upwind sources of the pollutant (or a strong background value) that must be subtracted from the horizontal advective flux.





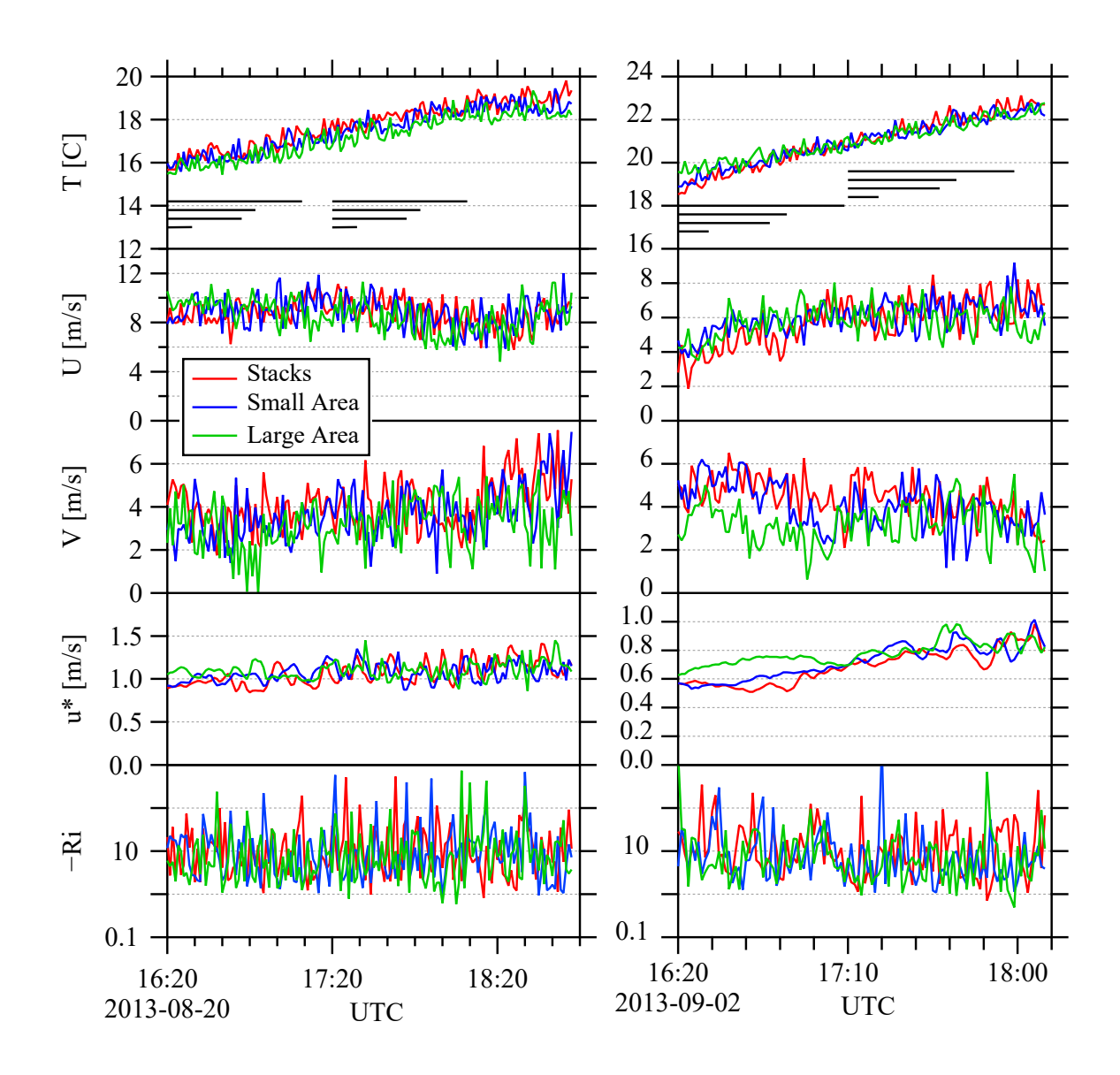


Figure 2: Meteorological variables during the model runs at 3 locations: (red) stacks, (blue) centre of small area sources, (green) centre of large area source. Temperature (T) and winds (U,V) are at a height of 150 m. Friction velocity (u_*) and negative bulk Richardson number (-Ri) are shown. The bulk Richardson number is based on a 10-m to 150-m height difference. The straight lines on the T axis show flight durations. From shortest to longest lines, they are: 10 instantaneous flights (spanning 9 minutes), stack flights, small area flights, and large area flights.

For the stack (i.e. point) sources, the calculation of the screen length based on an assumed $\pm 30^{\circ}$ lateral plume spread means that the screen length is approximately 1/6 of a total circle circumference. The difference in distance from the source



310

315

320

325

330

335



between a circle arc (radius R) and a straight line over a $\pm 30^{\circ}$ range is less than 7% of R. Hence the only significant differences between a spiral or cylinder flight and the downwind screens investigated here would be the extra time required to complete the remaining 5/6 of the circle for each transect (assuming no upwind sources or background concentration). For the stack emissions, we can investigate the difference in emissions estimates by using the same screen configuration, but we add a time offset after each transect to account for the time required to complete the flight path around the source.

We compare the difference between the screen flights and a circular enclosed flight pattern for a downwind distance of D = 10 km for the stack sources only. For the stack sources, the screen length at D = 10 km is L = 10 km. Thus, each screen transect (at a speed of 100 m/s) takes 100 seconds. For the circular enclosed flight comparison, we recalculate the flight, adding a 500 second offset to each transect to account for the time required to complete the loop. The flight time required (for all 10 circular enclosed flights) is 91 minutes in total (16:20 to 17:51 UTC), effectively spanning most of the model output duration and overlapping with both the 16:20 and 17:20 or 17:10 flights (Figure 2).

3 Results and Discussion

3.1 Stack Sources

3.1.1 Optimizing Screen Flights for D

Figure 3 shows the calculated horizontal advection fluxes (E_H , Eq. 2) for screens at given downwind distances (D) for the 4 cases: Aug 20 at 16:20 and 17:20, and Sept 2 at 16:20 and 17:10. The fluxes are calculated for the emissions from the 4 stacks (CNRL1-4) and are normalized by these known emissions (E_S). Each calculated advection flux (E_H/E_S) is the average of 10 flights. The standard deviation of E_H/E_S from the 10 flights is shown as both error bars on the average values and absolute values (to clearly demonstrate how σ changes with D). For clarity, in the discussion below all values of E_H/E_S are given as a ratio (e.g. 1.0), while all values of the standard deviation are given as percentages (e.g. 10%).

At a downwind distance of 2 km the instantaneous screen captures nearly all the stack emissions, with E_H/E_S values ranging from 0.90 and 0.98. This ratio generally increases with downwind distance, except for the Sep 2 17:10 flights. Deviation from a ratio of $E_H/E_S = 1$ may be due to uncertainty in the mean (which ranges from 0.10 to 0.25 for these results at a 95% CI), or one (or more) of the 7 other terms on the right side of Equation 2 may be non-negligible. As demonstrated in Fathi et al. (2023) there is negative mass creation in the model near the plume emission point (where concentration gradients are large) due to the turbulent diffusion scheme. This is generally consistent with the slight underestimation near the source and the increase in E_H/E_S with downwind distance (for 3 of the 4 cases).

At a downwind distance of 2 km, there is substantial variation between the instantaneous flights (σ ranges from 28% to 41%). Further from the source, σ generally decreases with D, with values ranging from 19% to 28% at a downwind distance of 10 km. From Equation 2, there may be some variation in horizontal turbulent flux (E_{HT}) for different flights. Fathi et al. (2023) estimated E_{HT} as < 0.4% and < 1.8% of E_S for Aug 20 and Sep 2 respectively. Since the screen captures the full



350



vertical extent of the plume, E_V and E_{VT} (flux through the box top) should be zero. There is no deposition or chemistry in the model, so E_{VD} and E_X are zero. E_M (the change in mass within the volume due to density change) is zero, since the screen is an instantaneous snapshot. Hence, this substantial variation between flights must be due to storage, with changes in wind speed and direction temporarily changing the advection flux through the screen (i.e. accumulation or subsequent release of pollutant between the stack and the screen). The storage terms estimated for 8 flights in Fathi et al. (2021), excluding a rejected flight, varied from -27% to 20%, which is comparable in scale to the variation seen between instantaneous cases here.

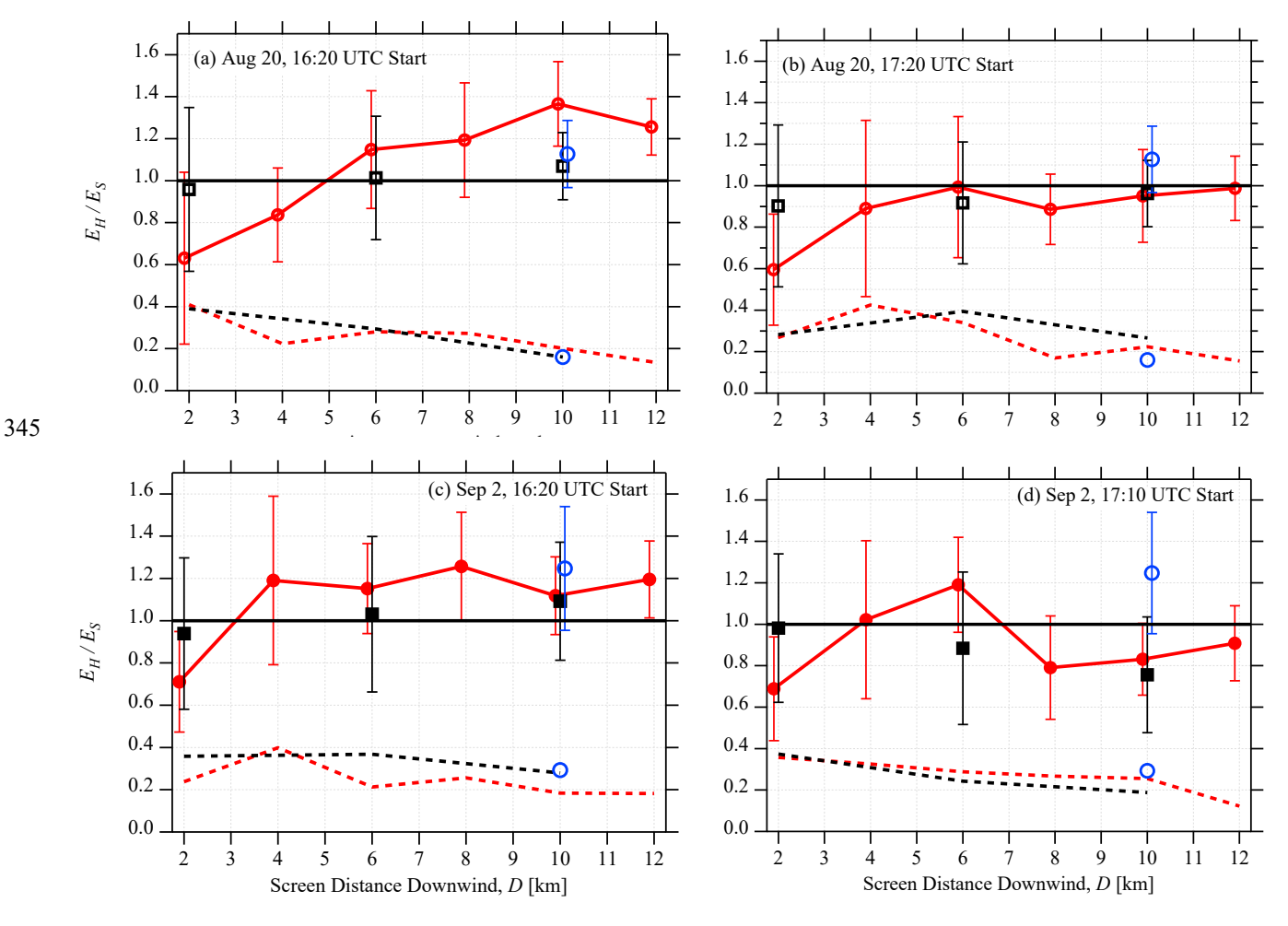


Figure 3. The variation in the ratio of horizontal advection flux (E_H) to the known emission rate (E_S) with downwind screen distance (D) for the 4 flight cases: Aug 20, starting 16:20 and 17:20, and Sep 2, starting 16:20 and 17:10. The black squares are the "instant" E_H/E_S values and red circles are the flights through the model (assuming a constant value between the lowest flight path at 150-m and the surface). Error bars show one standard deviation (σ) calculated from 10 flights (offset horizontally for clarity). The dashed lines show σ as absolute values to highlight the change in σ with D. The blue circles are the same variables (E_H/E_S) and σ 0 for 2 enclosed cylindrical flight patterns (on Aug 20 and Sep 2) starting at 16:20 and ending at 17:51.



355

360

365

370

375

380



For the non-instantaneous flights, which include uncertainty due to kriging interpolation and the extrapolation below the lowest flight path height in addition to the uncertainty of storage, the emission rate near the source (at D=2 km) is underestimated by the horizontal advective flux in all cases (ranging from 0.60 to 0.71). Further from the source, at D=6 km, the emissions are either nearly correct (0.99) or overestimated (up to 1.19). Beyond $D \ge 8$ km, the estimations vary considerably for different cases (ranging from 0.79 and 1.37). Much of this underestimation and overestimation is likely due to the extrapolation to the surface below the lowest flight path. Figures 4a-d show the profiles of the instantaneous flights, averaged for all 10 flights across the entire flight length. At D=2 km, the plume concentration below 150 m increases with concentration towards the surface, which results in an underestimation of the emission rate (lower than the underestimation of the instantaneous results in all cases). At D=6 km, there is some decrease in concentration towards the surface in 3 of the 4 cases, which results in an overestimation of E_S for that flight. At D=10 km, the concentration is nearly constant with height for the Sep 2 flights, although there is still substantial variability for the Aug 20 flights.

The standard deviation of E_H/E_S generally decreases with downwind distance, from as high as 41% at D=2 km to 12% at D=12 km. The standard deviations of the instantaneous, known flights for the same downwind distances is similar in magnitude to the variability in the flown sampled flights, suggesting that no substantial variability is added due to either the extrapolation below the lowest flight path, the kriging interpolation of the sparse sampling, or the sampling over an extended period of time (as opposed to an instantaneous snapshot). The decrease in variability with downwind distance suggests that uncertainty in individual flight estimations can be reduced with greater downwind distance, likely due to increased mixing and dispersion with downwind distance and the resulting smoothing of the plume across a larger area.

The estimation of E_S is generally higher in the non-instantaneous flight, relative to the instantaneous flights, for $D \ge 6$ km. This may be due to the kriging interpolation causing an overestimation of the screen concentrations. To test the interpolation, the concentration screen of the first single instantaneous Aug 20 flight (at 16:20) at D = 6 km was sampled using a typical flight path and then interpolated (and extrapolated below 150 m with constant values) to compare against the original screen. It was found that above 150 m, the kriging screen overestimated the average concentration of the original screen by 15%. The extrapolated concentrations below 150 m were overestimated by an average of 29% (consistent with the concentration profile at D = 6 km shown in Figs. 4a, which is an average of all 10 flights).

The non-instantaneous emission estimates may also be higher than the instantaneous emission estimates due to oversampling of a vertically moving plume. If the plume is moving in the same direction as the sampling (upwards in these cases), then the aircraft can sample the same plume multiple times. Conversely an opposite moving plume (downward for upward sampling) will result in under-estimation relative to the instantaneous estimates. This effect should be reduced with downwind distance as the plume becomes more vertically mixed and spread across a larger height range.





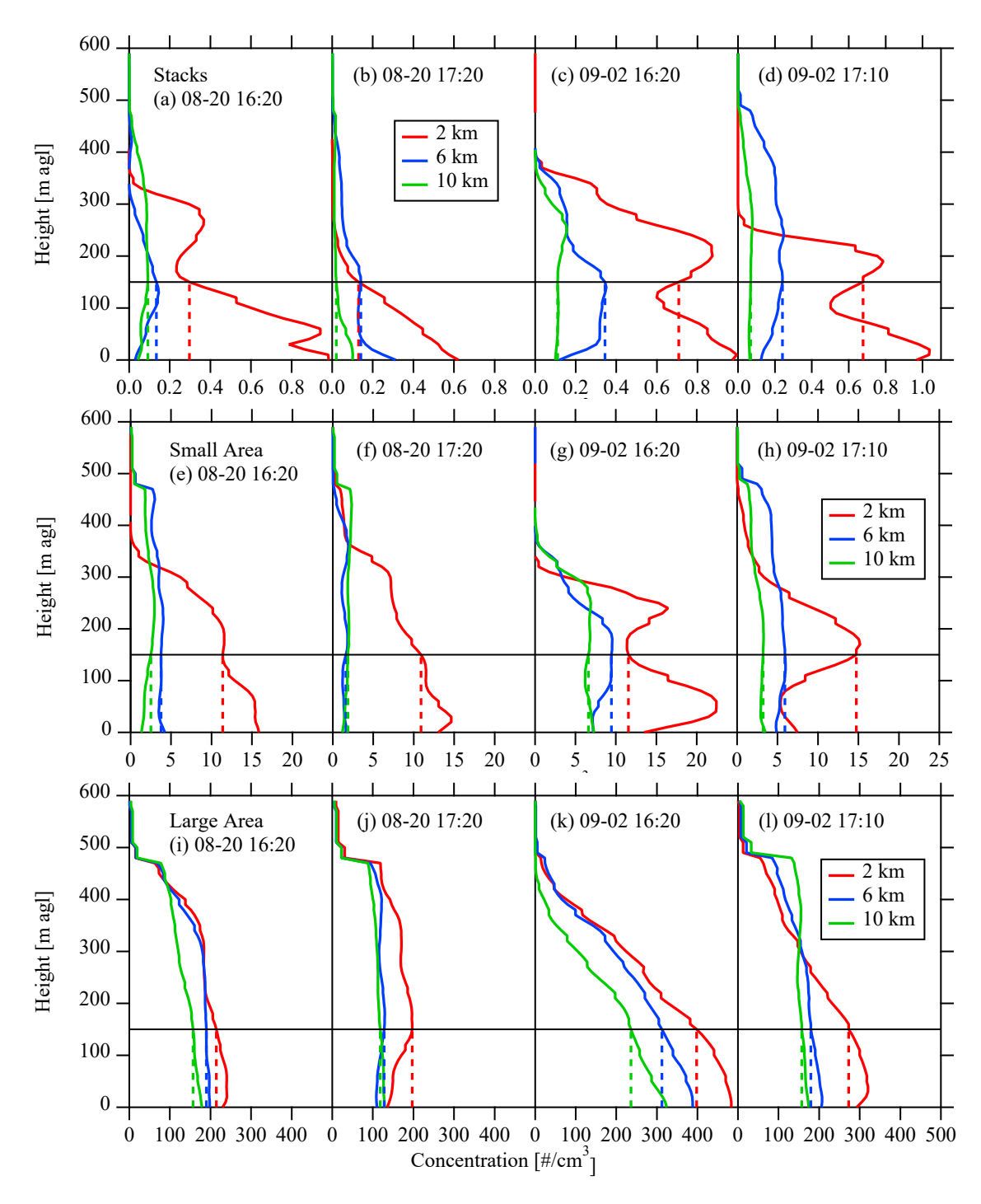


Figure 4. The concentration profiles from the instantaneous screens for the 4 flight cases and 3 source types at various downwind distances. These profiles are ensemble averages of 10 flight profiles averaged across the flight length (L) at each height. The dashed lines compare constant concentration below the lowest flight path (at $z_l = 150$ m).





390

395

400

405

410

415

420

The results demonstrate that it is difficult to determine an optimal flight distance, since there are multiple criteria that include optimization of E_H/E_S , reduction of σ , or correct extrapolation below the lowest flight path, and it will depend on the goals of the investigation. Generally, flying too close to the source (D = 2 km) results in an underestimation of the emission rate. For $D \ge 4$ km, the variation between flights decreases with distance, reaching approximately half its value at 10 km (relative to the value at D = 4 km). Flying at a downwind distance of D = 10 km, generally results in a constant concentration below the lowest flight path, but the results are still inconsistent at this distance. At a distance of D = 10 km, the emission rate at D = 10 km varies from 0.83 to 1.37, and the uncertainty in a single flight (S.E. with D = 10 km that D = 10 km varies from 0.83 to 1.37, and the uncertainty in a single flight (S.E. with D = 10 km that D = 10 km varies from 0.83 to 1.37, and the uncertainty in a single flight (S.E. with D = 10 km varies from 0.83 to 1.37, and the uncertainty in a single flight (S.E. with D = 10 km varies from 0.83 to 1.37, and the uncertainty in a single flight (S.E. with D = 10 km varies from 0.83 to 1.37, and the uncertainty in a single flight (S.E. with D = 10 km varies from 0.83 to 1.37, and the uncertainty in a single flight (S.E. with D = 10 km varies from 0.83 to 1.37, and the uncertainty in a single flight (S.E. with D = 10 km varies from 0.83 to 1.37, and the uncertainty in a single flight (S.E. with D = 10 km varies from 0.83 to 1.37, and the uncertainty in a single flight (S.E. with D = 10 km varies from 0.83 to 1.37, and the uncertainty in a single flight (S.E. with D = 10 km varies from 0.83 to 1.37, and the uncertainty in a single flight (S.E. with D = 10 km varies from 0.83 to 1.37 t

3.1.2 Optimizing Screen Flights for T

To further optimize the emission estimation as a function of flight time, we test the sensitivity of E_H/E_S to the vertical spacing of the transects at a downwind distance of D=10 km. For simplicity, we only compare 2 cases: Aug 20 and Sep 2 with 16:20 flight start times. Figure 5 demonstrates the variation in E_H/E_S with transect spacing. For the Aug 20 flights, emissions are overestimated by a factor between 1.27 and 1.32 with no dependence on T. For the Sep 2 flights, the emissions estimate ratio decreases with transect spacing from 1.15 at T=50 m to 0.94 at T=200 m. The variability shows no strong pattern with T and is lowest at a 150-m spacing (18%) for the Aug 20 flights, and at a 100-m spacing (15%) for the Sep 2 flights. For the Aug 20 flights, there is little dependence on T for either E_H/E_S and σ , suggesting that spacing could optimally be increased to 150 m or 200 m to reduce flight time; however for the Sep 2 flights, the ratio E_H/E_S changes significantly with increased spacing, suggesting that spacing of T>100 m will modify the emissions estimation and result in underprediction. This transition from overestimation at small spacing to underestimation at larger spacing could be due to vertical movement of the plume opposite to the sampling direction, resulting in transects missing the plume centre at larger spacing.

3.1.3 Comparing Enclosed Circular Flights

The results form the screen flights show that different conditions at different times of day can lead to error in the emissions estimation, most likely due to storage and release. As discussed above, sometime enclosed flight designs are necessary. The enclosed flight designs extend the flight time due to the time required to complete the circuit. For our investigated cases here, 2 circular enclosed flights span the flight times of the two screen flight times on each day. On Aug 20, the 16:20 screen flight at D = 10 km (Fig. 3a) overestimates the emissions (1.37), while the 17:20 screen flight (Fig. 3b) underestimates the emissions (0.95). The circular enclosed flight (Figs. 3a and b) is in the middle of these values (1.13), as might be expected since the sampling is spread out over a longer time. However, this is not the case for the Sep 2 flights. On Sept 2, the 16:20 screen flight at D = 10 km (Fig. 3c) similarly overestimates the emissions (1.12), while the 17:10 screen flight (Fig. 3d) underestimates the emissions (0.83), but the circular enclosed flight (Figs. 3c and d) overestimates the emissions (1.26) more





than the 16:20 screen flight. For both days, the variability (16% and 29%) is not substantially different from the variability of the screen flights. Hence, based on this analysis, we cannot conclude that the longer sampling time of the enclosed circular flights modifies the sampling efficiency in any predictable way.

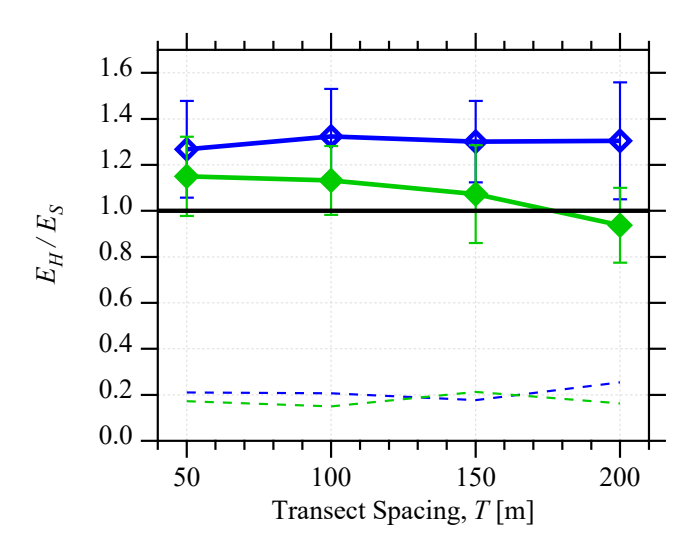


Figure 5. The variation in horizontal advection flux (E_H) to the known emission rate (E_S) with transect spacing (T) for both the Aug 20 (blue, open symbols) and Sep 2 (green, closed symbols) cases with 16:20 flight start times. Error bars and dashed lines show one standard deviation (calculated from 10 flights).

3.2 Area Sources

425

430

435

440

3.2.1 Optimizing Screen Flights for D

The analysis described above was repeated for the small area (mines) and large area (tailings pond) sources. These sources emit uniformly from the surface within the areas shown in Figure 1. The resulting horizontal advective fluxes (normalized by the known emission rates) are shown for the small area sources in Figs. 6a-d and for the large area source in Figs. 7a-d. The instantaneous results are inconsistent for the different sources and flights, suggesting that storage may affect the advective fluxes significantly. For the small area sources (Figs. 6a-d), the instantaneous flight horizontal advective fluxes underestimate (or slightly overestimate) the emission rate close (D = 2 km) to the source, ranging from 0.74 to 1.01. Beyond this distance, E_H/E_S ranges from 0.87 to 1.15. The non-instantaneous flights closely estimate the emissions in most cases, except for the Sep 2 16:20 case, where the emissions are overestimated. For the large area sources on Aug 20 (Figs. 7a-b), the emissions estimates are generally consistent, ranging from 0.91 to 1.18 (for both instantaneous and non-instantaneous flights). The Sep 2 flights (Figs. 7c-d) show a strong dependence on D, with both instantaneous and non-instantaneous flights showing similar values. Opposite patterns are seen for the Sep 2 16:20 flights (Fig. 7c), emissions are overestimated near the source for D < 10 km and underestimated for $D \ge 10 \text{ km}$. For the Sep 2 17:10 flights (Fig. 7d), emissions are nearly



450

455



1.0 near the source for $D \le 4$ km, underestimated for $6 \le D \le 10$ km and overestimated at D = 12 km. This implies that high variability in winds in these cases is leading to storage and release, resulting in build-up and subsequent release of pollutants at different distances downwind of the source. The relatively good agreement between instantaneous and non-instantaneous estimates implies that vertical motion of the plume does not result in over- or under-sampling.

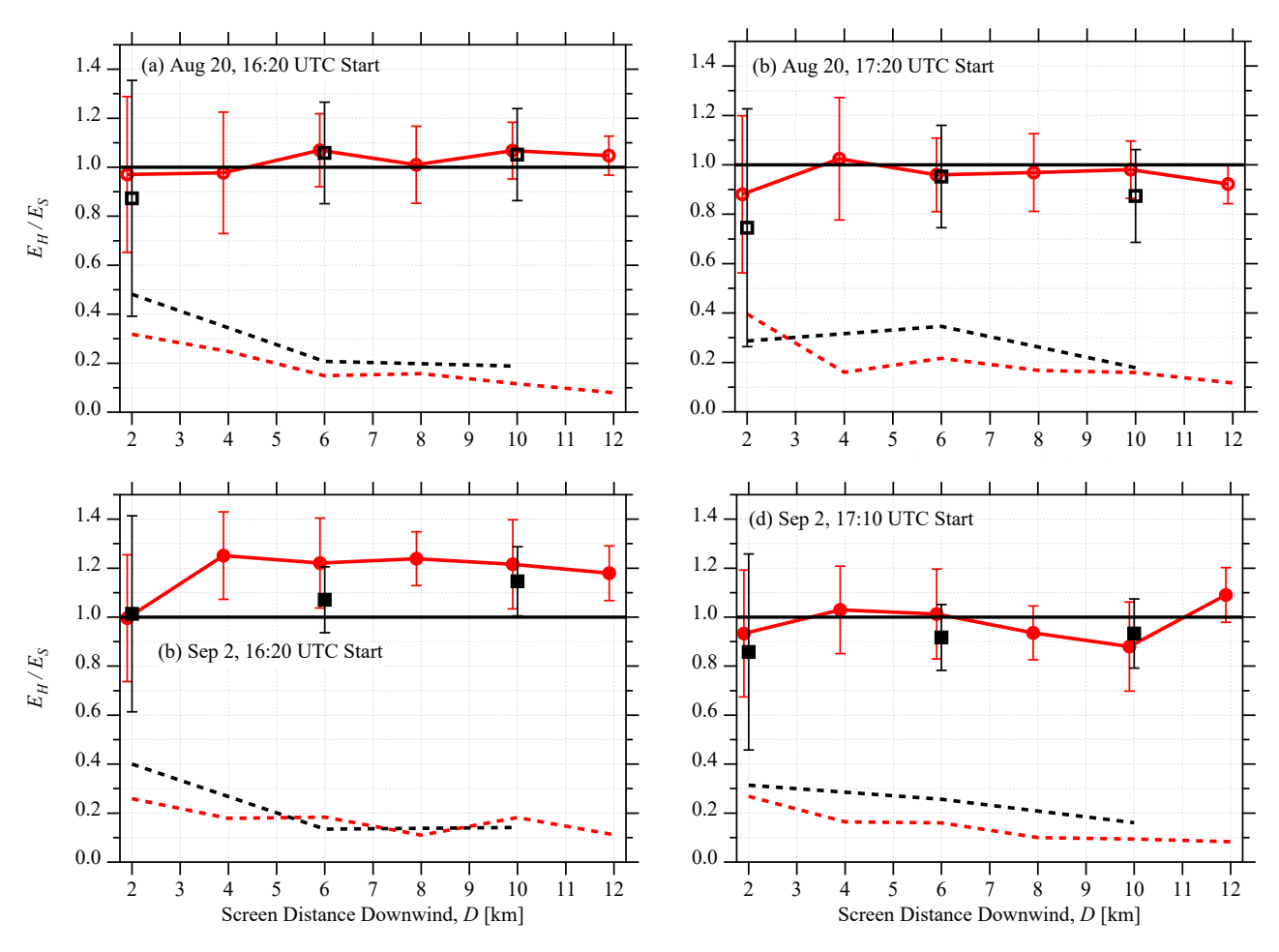


Figure 6. As Figure 3 for the flights downwind of the small area sources. Error bars and dashed lines show one standard deviation (calculated from 10 flights).

For the small area sources (Figs. 6a-d), the variability between the flights is consistently reduced with distance from the source, ranging from 26% to 48% at D = 2 km to between 8% and 12% at D = 12 km. The variability of the large area source measurements is much lower and does not consistently decrease with D, with values ranging from 2% to 13%. The lower variation for the large area source is expected since the wide plume from such a large area would be much less susceptible to wafting and the smaller-scale variation due to local wind effects. This indicates that a single flight sampling a



465

470



large area source would show substantially less uncertainty relative to a single flight sampling small area sources. For example, at D = 6 km, we expect an uncertainty (based on the variability between flights) of 16% for the large area source, compared to 43% for the small area sources.

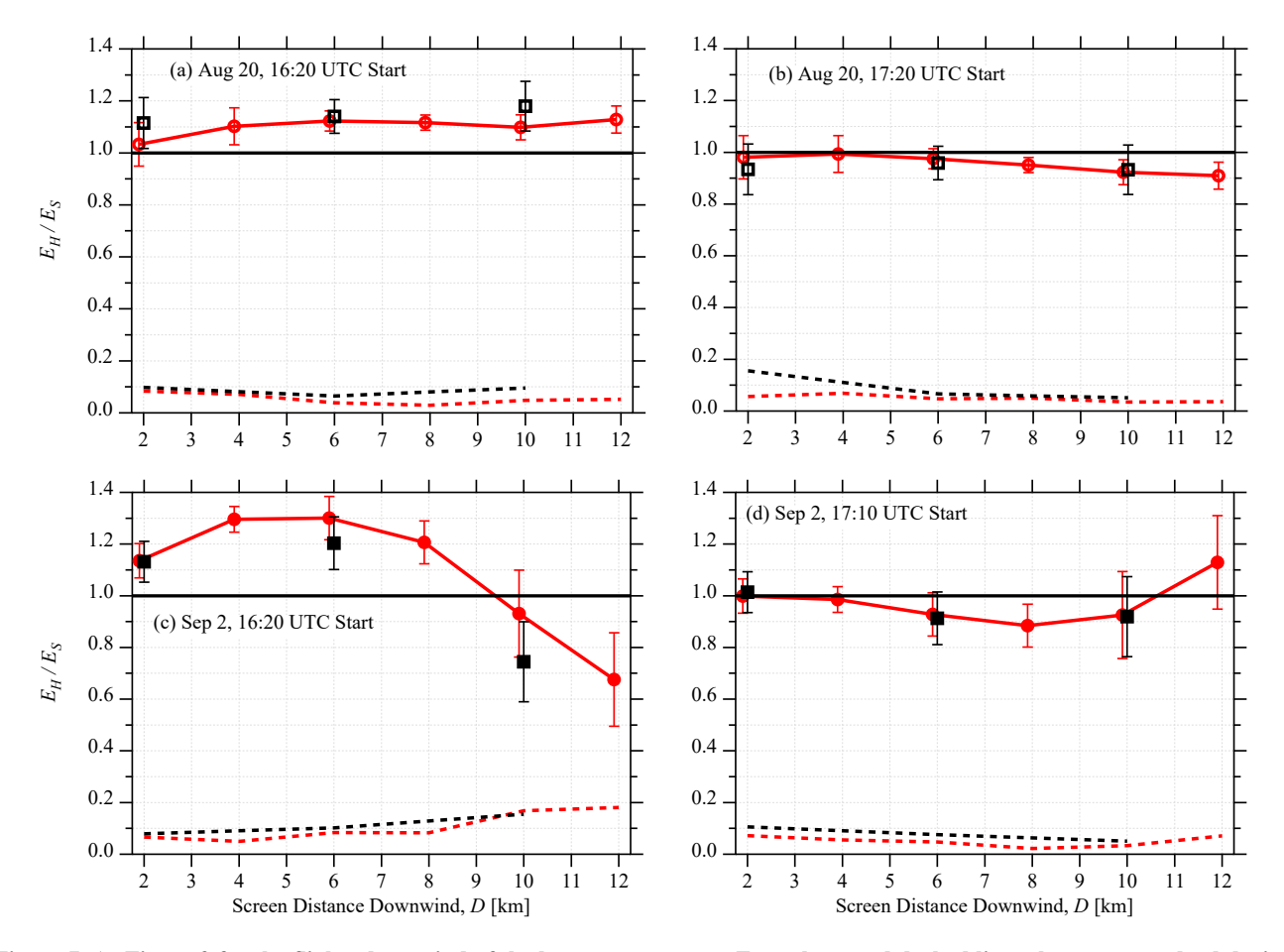


Figure 7. As Figure 3 for the flights downwind of the large area sources. Error bars and dashed lines show one standard deviation (calculated from 10 flights).

The concentration profiles from the instantaneous area source flights are shown in Figure 4(e-1), where they are compared to the extrapolation of a constant concentration below the lowest flight path. For the small area sources (Figs. 4e-h), the concentration is nearly constant below 150 m at D = 6 km for Aug 20, but it is overestimated by the constant extrapolation at D = 6 km for Sep 2. At D = 10 km, the concentration is nearly constant for all except the Aug 20 16:20 case, where it is overestimated by the extrapolation. For the large area source, the profiles for the Aug 20 flights (Figs. 4i-j) approach constant below the lowest flight path at D = 6 km; however, at 10 km downwind the concentration increases toward the ground for the 16:20 flights. For the Sep 2 flights at 16:20 (for the large area source), the profiles (Fig. 4k) do not deviate





from an exponential increase towards the surface at all distances, while for the 17:10 flights, they approach nearly constant at D = 10 km (with a slight underestimation by the extrapolation). It would be expected that an underestimation due to extrapolation (most prominent for the Sep 2 17:10 flights) would result in an underestimation of the emission rate for the non-instantaneous flights (relative to the instantaneous flights); however, this is not seen in Figure 7c, where the instantaneous advection flux is lower than the non-instantaneous advection flux (which includes the extrapolation).

As with the flights sampling the stack sources, it is difficult to determine an optimized downwind distance for these flights.

For the small area sources, the minimum distance with consistent emission estimation, minimum variability, and close to constant concentration below 150 m is D = 6 km; however, the non-constant concentrations below 150 m during the Sep 2 flights (at D = 6 km) suggests that the optimized value of D may be further downwind in some circumstances. For the large area sources, there is little variation in the concentration profile shape with downwind distance and the variance between flights is relatively small and independent of downwind distance. For this source, we can suggest an optimum downwind distance of D = 4 km. However, it is noted that, for both sources, the horizontal advection flux (E_H) differs significantly from the known emission rate (E_S), with factors between 0.96 and 1.22 for the small area sources (at D = 6 km) and between 0.99 and 1.30 for the large area sources (at D = 4 km). The overestimation is likely due to kriging errors or negative storage (release), or a combination of the two.

3.2.2 Optimizing Screen Flights for T

500

Using these optimal downwind distances (6 km and 4 km), we investigate the change in estimated emissions with transect spacing, T using only the 16:20 flights. For the small area source (at D=6 km), there is no change in E_H/E_S (≈ 1.06) with T for the Aug 20 flights (Fig. 8a); however, the variance between flights increases from 11% at T=50 m to 19% at T=200 m. For the Sep 2 flights, E_H/E_S decreases with increasing T, from 1.29 to 1.02, and the variance is lower at T=50 m (10%) and highest at T=100 m (20%). These results suggest that the uncertainty due to variation between flights can be minimized with a 50 m spacing; however, the emission rate estimation for the Sep 2 flights at this spacing is high ($E_H/E_S=1.29$). Increasing the spacing to 200 m will reduce the flight time by a factor of 4 but nearly doubles the uncertainty due to variation between flights.

The variation of E_H/E_S and σ with T for the large area source (Fig. 8b) is similar to the variation seen for the small area source. For the Aug 20 flights, E_H/E_S increases with T, from 1.08 at T=50 m to 1.15 at T=150 m and the variance increases from 6% at T=50 m to 10% at T=200 m. For the Sep 2 flights, E_H/E_S decreases with increasing T, from 1.31 to 1.26, and the variance ranges from a minimum of 4% at T=50 m to \sim 7% for other values. Similar to the small area source, the spacing is optimized (based on variation between flights) at 50 m or 100 m but increasing the spacing to 200 m increases the uncertainty from 6 to 10% (Aug 20) or 4% to 6% (Sep 2), which could be acceptable depending on the required accuracy and the cost of flight time.





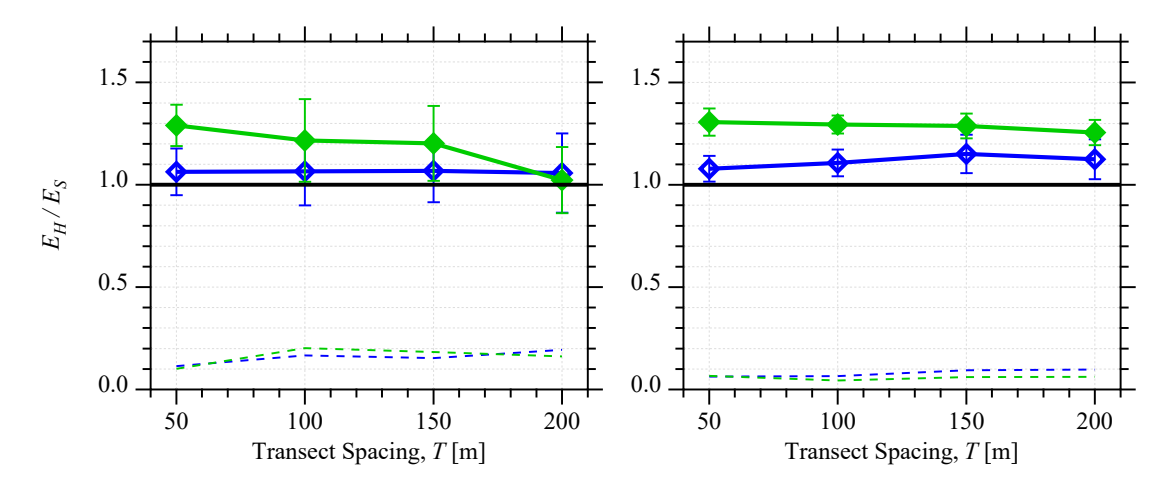


Figure 8. As Figure 5 for the flights downwind of the small (a) and large (b) area sources. Aug 20 shown as blue, open symbols, and Sep 2 shown as green, closed symbols.

3.3 Scaling

505

525

Following Conley et al. (2017), we non-dimensionalize the downwind distance following Equation 1 (with D' and D instead of R' and R). As with Conley et al. (2017), we approximate the convective flux as $w_* = \sigma_U/0.6$, where σ_U is the standard deviation of the wind speed. The boundary-layer heights are taken as $z_i = 470$ m for the Aug 20 flights, and $z_i = 480$ m for the Sep 2 flights, as can be inferred from the profiles in Figure 4. The boundary layer heights are assumed not to change significantly during the duration of the flights. Using these values with the average wind speeds for each flight duration, D' is calculated for each set of 10 flights.

Figures 9a and 9b compare the emission flux estimates and variation for all the sources for both dimensionalized downwind distance, D (Fig. 9a), and non-dimensionalized downwind distance, D'(Fig. 9b). The results are not collapsed due to non-dimensionalization as substantial variation is seen in the results using either D or D'. There is significant variability in the average values of E_H/E_S for all sources over a wide range of D' values, and the results do not asymptote to a value of E_H/E_S = 1.0. For the small area sources, the standard deviation, σ (the variability between the 10 flights) is lowest for D' ≥
6, while for the large area source flights it is smallest over the range 2 ≤ D' ≤ 4. For the stack source flights, σ tends to decrease with D', but there is no apparent minimum or asymptotic D' value.

We also investigate the effect of non-dimensionalization on the accuracy of the constant concentration extrapolation below the lowest flight path. The average concentration below the lowest flight path <C> is calculated from the instantaneous flights (see Fig. 4) and this is normalized by the extrapolated concentration at the lowest flight path level, $C(z_l)$, where $z_l = 150$ m. When the results are non-dimensionalized, <C>/ $C(z_l)$ varies from 0.79 to 1.22 for $D' \ge 3$, suggesting that the extrapolation should be within approximately 20% beyond that distance. However, this analysis ignores the significant





overestimation of <C> for the Aug 20 17:20 stack flights at D=10 km (see Fig. 4b), and it is unclear what would happen at further downwind distances for that flight.

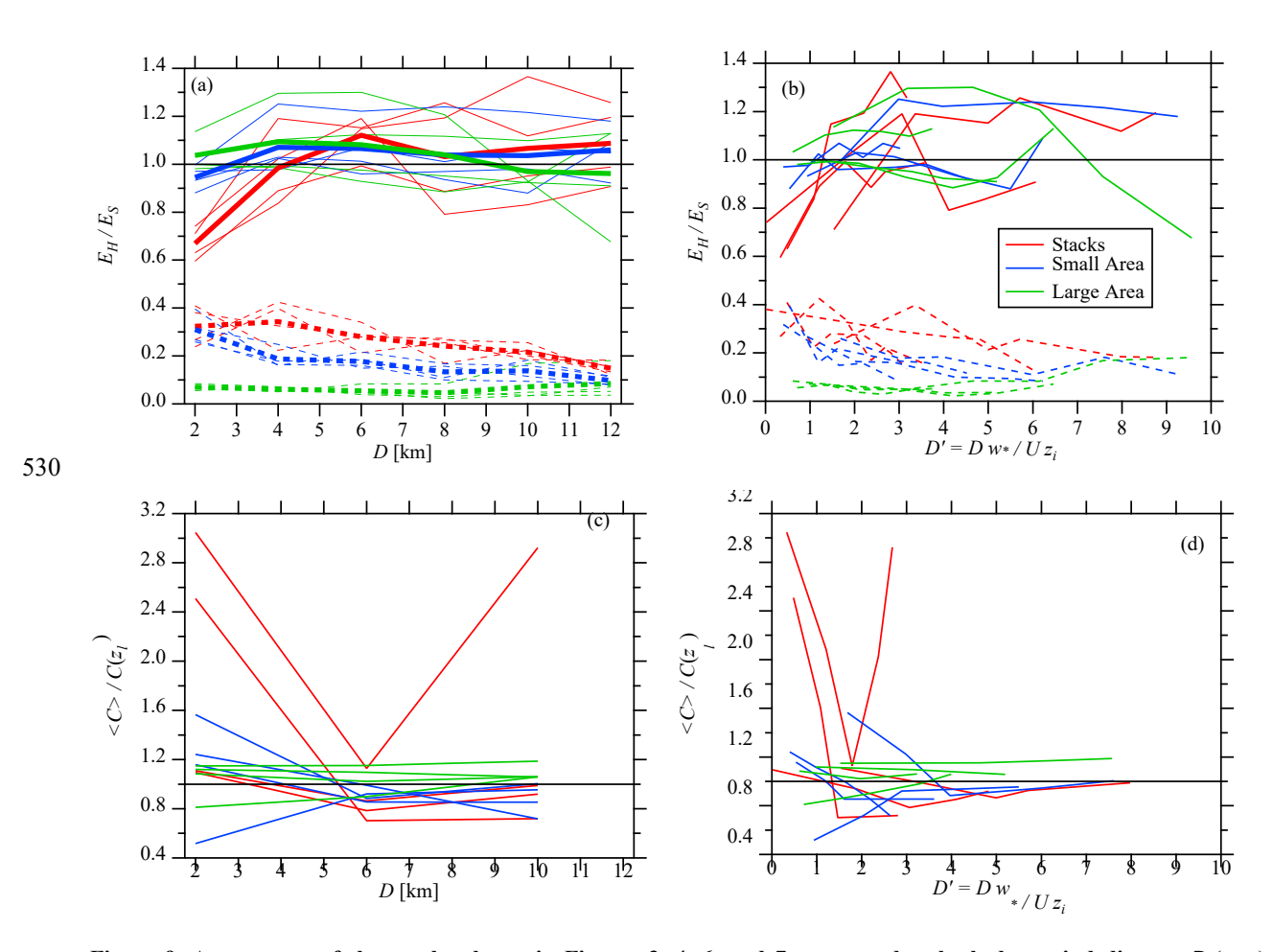


Figure 9. A summary of the results shown in Figures 3, 4, 6, and 7, compared to both downwind distance D (a, c), and non-dimensionalized downwind distance, D' (b, d). Panels (a) and (b) show the ratio of estimated advection flux, E_H , to the known emission rate, E_S , and the standard deviation of the ratio, σ . In Panel (a), the thicker line is the average of all 4 flight times. Panels (c) and (d) show the ratio of average concentration below the lowest flight level ($z_l = 150$ m) to the constant concentration extrapolation (see Fig. 4).

4 Conclusions

535

540

The results of this study demonstrate that emissions estimates can be substantially varied under different conditions. This reinforces the importance of storage and release discussed in Fath et al. (2021) and Fathi et al. (2023). A vertically moving (rising or falling) plume may also lead to under- or over-estimation of the emissions for the non-instantaneous flight,



545

550

555

560

565

570



although this would not explain under- or over-estimation in the instantaneous flights. Further uncertainty is introduced by the kriging interpolation, which is shown in one case (for stack sources) to overestimate the average concentration by 15% (using an instantaneous flight example).

When all the different flight times are averaged, the storage/release conditions tend to cancel and the average E_H values are within 12% of E_S for a downwind distance of 4 km or more. Hence, based on the average estimate of E_H/E_S alone, a screen at a downwind distance of 4 km or more provides the same level of accuracy for the three types of sources investigated here (i.e. elevated stacks, small surface area sources, or a large surface area source).

However, variability between individual flights is a very large source of uncertainty. This variability is likely due to changes in storage/release over the flight times, since similar variability is seen instantaneous results. At a downwind distance of 4 km, for elevated stack sources, this variability between flights can be as much as $\sigma = 42\%$, which suggests an uncertainty of 82% (at a 95% CI) in that particular case. At the same distance, variability for the surface area sources is much less ($\sigma = 25\%$ for small area sources, and 7% for the large area source). The variability between flights tends to decrease with increasing downwind distance. For the stack and small area sources, σ reaches half the D=4 km value between D=10 and 12 km. However, flight time also increases with downwind distance. For the case of the stack sources, the screen at 12 km takes 3 times as long to complete as the screen at 4 km (since L=D for the smokestack screens). Hence, 3 flights can be flown at D=4 km in the same time it takes to fly one flight at D=12 km. Taking the average of these 3 flights, reduces the uncertainty by a factor of 0.58 ($1/\sqrt{3}$). Hence, comparable accuracy can be achieved by taking multiple flights closer to the source relative to a single flight further downwind. This is not the case for the large area source, where the variation is small and reaches a minimum (average $\sigma = 5\%$) at D=8 km. For this source type, increasing the downwind distance of the screen does not reduce uncertainty due to variability between flights.

For elevated stack sources, the results show that reducing the transect spacing below 100 m does not offer any benefits in emission estimation, but increasing the space beyond 150 m can increase uncertainty and modify the E_H estimates. For area sources, the variability between flights is minimized with a transect spacing of T = 50 m. For small area sources, increasing the spacing to 200 m (reducing flight time by a factor of 0.25) doubles the uncertainty, while for the large area source, increasing the spacing to 200 m increases the uncertainty by a factor of ~1.5. As with the optimization of downwind flight distance, multiple flights with a larger transect spacing may results in similar uncertainties compared to a single flight at smaller transect spacing.

These results further demonstrate that one of the most substantial sources of error in the emissions estimate is due to the extrapolation of the results between the surface and the lowest flight path level (as outlined by Gordon et al., 2015 and Conley et al. 2017 for example). Extrapolation error is most significant close to the source, as would be expected, but it can be surprisingly persistent further downwind, in one flight case (for the stack sources), overestimating the concentration below 150 m by a factor of 3 at D = 10 km. For the area sources, the extrapolation error is less than 30% for distances of 4 km or greater. Non-dimensionalization of the results suggests that the extrapolation error is within 20% for non-dimensional

https://doi.org/10.5194/egusphere-2025-4542 Preprint. Discussion started: 30 October 2025

© Author(s) 2025. CC BY 4.0 License.



575

580

EGUsphere Preprint repository

distance of $D' \ge 3$, with the caveat that more results at this distance are required to confirm this result. These results

emphasize the need to constrain aircraft measurements with coincident surface or near-surface measurements whenever

possible. Substantial improvements in emission estimation accuracy can be achieved by mobile vehicle, UAV, or remote

sensing (e.g. lidar) sampling beneath the aircraft.

The results demonstrate that it is difficult to provide a single optimized distance and transect spacing given the variability of

conditions and the effects of storage and release. However, the results do demonstrate the potential to improve emission rate

retrieval by accompanying any flight campaign with a strong modelling effort. This approach seems to be the only way to

account for storage and release once the campaign is complete. Reanalysis data combined with tracer release can be used to

mimic flight actual patterns and estimate storage and release during actual flight time, thus reducing the most substantial

uncertainty in the emission rate estimation.

Author Contribution

585 SF set up and ran all the WRF modelling. SF and MG designed the experiments using the WRF model output, performed the

analysis, and wrote the manuscript. JH provided code for WRF output analysis.

Competing Interests

The authors declare that they have no conflict of interest.

Financial Support

590 Funding to MG and SF provided by the NSERC Discovery Grant (RGPIN-2015-04292). Computational resources provided

by Digital Research Alliance of Canada (RRG #3535).

Code/Data availability

Code and data are available on request from the authors.

References

5 Alfieri, S., Amato, U., Carfora, M., Esposito, M., and Magliulo, V.: Quantifying trace gas emissions from composite

landscapes: A mass-budget approach with aircraft measurements, Atmospheric Environment, 44, 1866-1876,

https://doi.org/https://doi.org/10.1016/j.atmosenv.2010.02.026, 2010.





- Andreae, M. O., Acevedo, O. C., Araùjo, A., Artaxo, P., Barbosa, C. G. G., Barbosa, H. M. J., Brito, J., Carbone, S., Chi, X., Cintra, B. B. L., da Silva, N. F., Dias, N. L., Dias-Júnior, C. Q., Ditas, F., Ditz, R., Godoi, A. F. L., Godoi, R. H. M.,
- Heimann, M., Hoffmann, T., Kesselmeier, J., Könemann, T., Krüger, M. L., Lavric, J. V., Manzi, A. O., Lopes, A. P., Martins, D. L., Mikhailov, E. F., Moran-Zuloaga, D., Nelson, B. W., Nölscher, A. C., Santos Nogueira, D., Piedade, M. T. F., Pöhlker, C., Pöschl, U., Quesada, C. A., Rizzo, L. V., Ro, C.-U., Ruckteschler, N., Sá, L. D. A., de Oliveira Sá, M., Sales, C. B., dos Santos, R. M. N., Saturno, J., Schöngart, J., Sörgel, M., de Souza, C. M., de Souza, R. A. F., Su, H., Targhetta, N., Tóta, J., Trebs, I., Trumbore, S., van Eijck, A., Walter, D., Wang, Z., Weber, B., Williams, J., Winderlich, J., Wittmann, F.,
- Wolff, S., and Yáñez Serrano, A. M.: The Amazon Tall Tower Observatory (ATTO): overview of pilot measurements on ecosystem ecology, meteorology, trace gases, and aerosols, Atmospheric Chemistry and Physics, 15, 10 723–10 776, https://doi.org/10.5194/acp-15-10723-2015, 2015.
- Angevine, W. M., Peischl, J., Crawford, A., Loughner, C. P., Pollack, I. B., and Thompson, C. R.: Errors in top-down estimates of emissions using a known source, Atmospheric Chemistry and Physics, 20, 11 855–11 868, https://doi.org/10.5194/acp-20-11855-2020, 2020.
 - Baray, S., Darlington, A., Gordon, M., Hayden, K. L., Leithead, A., Li, S.-M., Liu, P. S. K., Mittermeier, R. L., Moussa, S. G., O'Brien, J., Staebler, R., Wolde, M., Worthy, D., and McLaren, R.: Quantification of methane sources in the Athabasca Oil Sands Region of Alberta by aircraft mass balance, Atmospheric Chemistry and Physics, 18, 7361–7378, https://doi.org/10.5194/acp-18-7361-2018, 2018.
- Bell, T. M., Klein, P. M., Lundquist, J. K., and Waugh, S.: Remote-sensing and radiosonde datasets collected in the San Luis Valley during the LAPSE-RATE campaign, Earth System Science Data, 13, 1041–1051, https://doi.org/10.5194/essd-13-1041-2021, 2021.
 - Brus, D., Gustafsson, J., Kemppinen, O., de Boer, G., and Hirsikko, A.: Atmospheric aerosol, gases, and meteorological parameters measured during the LAPSE-RATE campaign by the Finnish Meteorological Institute and Kansas State University, Earth System Science Data, 13, 2909–2922, https://doi.org/10.5194/essd-13-2909-2021, 2021a.
- Brus, D., Gustafsson, J., Vakkari, V., Kemppinen, O., de Boer, G., and Hirsikko, A.: Measurement report: Properties of aerosol and gases in the vertical profile during the LAPSE-RATE campaign, Atmospheric Chemistry and Physics, 21, 517–533, https://doi.org/10.5194/acp-21-517-2021, 2021b.
- Cambaliza, M. O. L., Shepson, P. B., Caulton, D. R., Stirm, B., Samarov, D., Gurney, K. R., Turnbull, J., Davis, K. J., Possolo, A., Karion, A., Sweeney, C., Moser, B., Hendricks, A., Lauvaux, T., Mays, K., Whetstone, J., Huang, J.,
- Razlivanov, I., Miles, N. L., and Richardson, S. J.: Assessment of uncertainties of an aircraft-based mass balance approach for quantifying urban greenhouse gas emissions, Atmos. Chem. Phys., 14, 9029–9050, doi:10.5194/acp-14-9029-2014, 2014. Conley, S., Faloona, I., Mehrotra, S., Suard, M., Lenschow, D. H., Sweeney, C., Herndon, S., Schwietzke, S., Pétron, G., Pifer, J., Kort, E. A., and Schnell, R.: Application of Gauss's theorem to quantify localized surface emissions from airborne
- 630 measurements of wind and trace gases, Atmospheric Measurement Techniques, 10, 3345–3358, https://doi.org/10.5194/amt-10-3345-2017, 2017.



635



- Davis, Z. Y. W., Baray, S., McLinden, C. A., Khanbabakhani, A., Fujs, W., Csukat, C., Debosz, J., and McLaren, R.: Estimation of NOx and SO2 emissions from Sarnia, Ontario, using a mobile MAX-DOAS (Multi-AXis Differential Optical Absorption Spectroscopy) and a NOx analyzer, Atmospheric Chemistry and Physics, 19, 13 871-13 889, https://doi.org/10.5194/acp-19-13871-2019, 2019.
- Davis, Z. Y. W., Frieß, U., Strawbridge, K. B., Aggarwaal, M., Baray, S., Schnitzler, E. G., Lobo, A., Fioletov, V. E., Abboud, I., McLin-den, C. A., Whiteway, J., Willis, M. D., Lee, A. K. Y., Brook, J., Olfert, J., O'Brien, J., Staebler, R., Osthoff, H. D., Mihele, C., and McLaren, R.: Validation of MAX-DOAS retrievals of aerosol extinction, SO2, and NO2 through comparison with lidar, sun photometer, active DOAS, and aircraft measurements in the Athabasca oil sands region,
- Atmospheric Measurement Techniques, 13, 1129-1155, https://doi.org/10.5194/amt-13-1129-2020, 2020. de Boer, G., Waugh, S., Erwin, A., Borenstein, S., Dixon, C., Shanti, W., Houston, A., and Argrow, B.: Measurements from mobile surface vehicles during the Lower Atmospheric Profiling Studies at Elevation – a Remotely-piloted Aircraft Team Experiment (LAPSE-RATE), Earth System Science Data, 13, 155–169, https://doi.org/10.5194/essd-13-155-2021, 2021.
- Fathi, S.: Optimizing Top-down Airborne Emission Retrievals through High and Super-Resolution Numerical Modelling, 645 Dissertation, http://hdl.handle.net/10315/40663 (last access: 4 July 2025), 2022.
 - Fathi, S., Gordon, M., and Chen, Y.: Passive-tracer modelling at super-resolution with Weather Research and Forecasting Advanced Research WRF (WRF-ARW) to assess mass-balance schemes, Geosci. Model Dev., 16, 5069-5091, https://doi.org/10.5194/gmd-16-5069-2023, 2023.
- Fathi, S., Gordon, M., Makar, P. A., Akingunola, A., Darlington, A., Liggio, J., Hayden, K., and Li, S.-M.: Evaluating the 650 impact of storage- and-release on aircraft-based mass-balance methodology using a regional air-quality model, Atmospheric Chemistry and Physics, 21, 15 461–15 491, https://doi.org/10.5194/acp-21-15461-2021, 2021.
 - Fiehn, A., Kostinek, J., Eckl, M., Klausner, T., Gałkowski, M., Chen, J., Gerbig, C., Röckmann, T., Maazallahi, H., Schmidt, M., Korbeń, P., Necki, J., Jagoda, P., Wildmann, N., Mallaun, C., Bun, R., Nickl, A.-L., Jöckel, P., Fix, A., and Roiger, A.: Estimating CH₄, CO₂ and CO emissions from coal mining and industrial activities in the Upper Silesian Coal Basin using an
- 655 aircraft-based mass balance approach, Atmos. Chem. Phys., 20, 12675–12695, https://doi.org/10.5194/acp-20-12675-2020, 2020.
 - Gordon, M., Li, S.-M., Staebler, R., Darlington, A., Hayden, K., O'Brien, J., and Wolde, M.: Determining air pollutant emission rates based on mass balance using airborne measurement data over the Alberta oil sands operations, Atmospheric Measurement Techniques, 8, 3745–3765, https://doi.org/10.5194/amt-8-3745-2015, 2015.
- 660 He, M.; Ditto, J. C.; Gardner, L.; Machesky, J.; Hass-Mitchell, T. N.; Chen, C.; Khare, P.; Sahin, B.; Fortner, J. D.; Plata, D. L.; Drollette, B. D.; Hayden, K. L.; Wentzell, J. J. B.; Mittermeier, R. L.; Leithead, A.; Lee, P.; Darlington, A.; Wren, S. N.; Zhang, J.; Wolde, M.; Moussa, S. G.; Li, S.-M.; Liggio, J.; Gentner, D. R.: Total organic carbon measurements reveal major gaps in petrochemical emissions reporting. Science, 383,426-432(2024), http://doi:10.1126/science.adj6233, 2024.





- Han, T., Xie, C., Liu, Y., Yang, Y., Zhang, Y., Huang, Y., Gao, X., Zhang, X., Bao, F., and Li, S.-M.: Development of a continuous UAV-mounted air sampler and application to the quantification of CO₂ and CH₄ emissions from a major coking plant, Atmos. Meas. Tech., 17, 677–691, https://doi.org/10.5194/amt-17-677-2024, 2024.
 - Hayden, K., Li, S.-M., Makar, P., Liggio, J., Moussa, S. G., Akingunola, A., McLaren, R., Staebler, R. M., Darlington, A., O'Brien, J., Zhang, J., Wolde, M., and Zhang, L.: New methodology shows short atmospheric lifetimes of oxidized sulfur and nitrogen due to dry deposition, Atmos. Chem. Phys., 21, 8377–8392, https://doi.org/10.5194/acp-21-8377-2021, 2021.
- Heintzenberg, J., Birmili, W., Otto, R., Andreae, M. O., Mayer, J.-C., Chi, X., and Panov, A.: Aerosol particle number size distributions and particulate light absorption at the ZOTTO tall tower (Siberia), 2006–2009, Atmospheric Chemistry and Physics, 11, 8703–8719, https://doi.org/10.5194/acp-11-8703-2011, 2011.
 - Hiller, R., Neininger, B., Brunner, D., Gerbig, C., Bretscher, D., Künzle, T., Buchmann, N., Eugster, W.: Aircraft-based CH4 flux estimates for validation of emissions from an agriculturally dominated area in Switzerland, *JGR Atmos.*, 119(8),
- 675 https://doi.org/10.1002/2013JD020918, 2014.
 - Islam, A., Shankar, A., Houston, A., and Detweiler, C.: University of Nebraska unmanned aerial system (UAS) profiling during the LAPSE- RATE field campaign, Earth System Science Data, 13, 2457–2470, https://doi.org/10.5194/essd-13-2457-2021, 2021.
- JOSM: Joint Oil Sands Monitoring Plan, Integrated Monitoring Plan for the Oil Sands, Air Quality Component, p. 72, http://publications.gc. ca/site/eng/394253/publication.html, 2013.
 - Karion, A., Sweeney, C., Pétron, G., Frost, G., Hardesty, R. M., Kofler, J., Miller, B. R., Newberger, T., Wolter, S., Banta, R., Brewer, A., Dlugokencky, E., Lang, P., Montzka, S. A., Schnell, R., Tans, P., Trainer, M., Zamora, R., and Conley, S.: Methane emissions estimate from airborne measurements over a western United States natural gas field, Geophys. Res. Lett., 40, 4393–4397, doi:10.1002/grl.50811, 2013.
- Karion, A., Lauvaux, T., Lopez Coto, I., Sweeney, C., Mueller, K., Gourdji, S., Angevine, W., Barkley, Z., Deng, A., Andrews, A., Stein, A., and Whetstone, J.: Intercomparison of atmospheric trace gas dispersion models: Barnett Shale case study, Atmospheric Chemistry and Physics, 19, 2561–2576, https://doi.org/10.5194/acp-19-2561-2019, 2019.
- Kalthoff, N., Corsmeier, U., Schmidt, K., Kottmeier, C., Fiedler, F., Habram, M., and Slemr, F.: Emissions of the city of Augsburg determined using the mass balance method, Atmos. Environ., 36, 19–31, https://doi.org/10.1016/S1352-690 2310(02)00215-7, 2002.
 - Kim J., Lee, G., Jun, J., Seo, B-K., Choi, Y., Quantification of SO2 and CO2 emission rates from coal-fired power plants in the Korean peninsula via airborne measurements, Sci. Tot. Env., 978, 179430, https://doi.org/10.1016/j.scitotenv.2025.179430, 2025.
- Kostinek, J., Roiger, A., Eckl, M., Fiehn, A., Luther, A., Wildmann, N., Klausner, T., Fix, A., Knote, C., Stohl, A., and Butz, A.: Estimating Upper Silesian coal mine methane emissions from airborne in situ observations and dispersion modeling, Atmos. Chem. Phys., 21, 8791–8807, https://doi.org/10.5194/acp-21-8791-2021, 2021.





- Krings, T., Neininger, B., Gerilowski, K., Krautwurst, S., Buchwitz, M., Burrows, J. P., Lindemann, C., Ruhtz, T., Schüttemeyer, D., and Bovensmann, H.: Airborne remote sensing and in situ measurements of atmospheric CO2 to quantify point source emissions, Atmos. Meas. Tech., 11, 721–739, https://doi.org/10.5194/amt-11-721-2018, 2018.
- Li, S.-M., Leithead, A., Moussa, S. G., Liggio, J., Moran, M. D., Wang, D., Hayden, K., Darlington, A., Gordon, M., Staebler, R., Makar, P. A., Stroud, C. A., McLaren, R., Liu, P. S. K., O'Brien, J., Mittermeier, R. L., Zhang, J., Marson, G., Cober, S. G., Wolde, M., and Wentzell, J. J. B.: Differences between measured and reported volatile organic compound emissions from oil sands facilities in Alberta, Canada, Proceedings of the National Academy of Sciences, 114, E3756–E3765, https://doi.org/10.1073/pnas.1617862114, 2017.
- Liggio, J., Li, S.-M., Staebler, R. M., Hayden, K., Darlington, A., Mittermeier, R. L., O'Brien, J., McLaren, R., Wolde, M., Worthy, D., and Vogel, F.: Measured Canadian oil sands CO2 emissions are higher than estimates made using internationally recommended methods, Nature Communications, 10, 1863, https://doi.org/10.1038/s41467-019-09714-9, 2019.
- Mays, K.L., Shepson, P.B., Stirm, B.H., Karion, A., Sweeney, C., Gurney, K.R.: Aircraft-Based Measurements of the Carbon Footprint of Indianapolis, Environ. Sci. Technol., 43, 20, 7816–7823, https://doi.org/10.1021/es901326b, 2009.
 - Nambiar, M. K., Byerlay, R. A. E., Nazem, A., Nahian, M. R., Moradi, M., and Aliabadi, A. A.: A Tethered Air Blimp (TAB) for observing the microclimate over a complex terrain, Geoscientific Instrumentation, Methods and Data Systems, 9, 193–211, https://doi.org/10.5194/gi-9-193-2020, 2020.
- Nygård, T., Tisler, P., Vihma, T., Pirazzini, R., Palo, T., and Kouznetsov, R.: Properties and temporal variability of summertime tem- perature inversions over Dronning Maud Land, Antarctica, Quarterly Journal of the Royal Meteorological Society, 143, 582–595, https://doi.org/https://doi.org/10.1002/qj.2951, 2017.
 - Onishi, R., Sugiyama, D., and Matsuda, K.: Super-Resolution Simulation for Real-Time Prediction of Urban Micrometeorology, SOLA, 15, 178–182, https://doi.org/10.2151/sola.2019-032, 2019.
- Panitz, H.-J., Nester, K., and Fiedler, F.: Mass budget simulation of NOx and CO for the evaluation of calculated emissions for the city of Augsburg (Germany), Atmos. Environ., 36, 33–51, 2002.
 - Peischl, J., Ryerson, T. B., Holloway, J. S., Parrish, D. D., Trainer, M., Frost, G. J., Aikin, K. C., Brown, S. S., Dubé, W. P., Stark, H., and Fehsenfeld, F. C.: A top-down analysis of emissions from selected Texas power plants during TexAQS 2000 and 2006, Journal of Geophysical Research: Atmospheres, 115, https://doi.org/https://doi.org/10.1029/2009JD013527, 2010. Ražnjević, A., van Heerwaarden, C., van Stratum, B., Hensen, A., Velzeboer, I., van den Bulk, P., and Krol, M.: Technical
- note: Interpretation of field observations of point-source methane plume using observation-driven large-eddy simulations, Atmos. Chem. Phys., 22, 6489–6505, https://doi.org/10.5194/acp-22-6489-2022, 2022.
 - Ryoo, J.-M., Iraci, L. T., Tanaka, T., Marrero, J. E., Yates, E. L., Fung, I., Michalak, A. M., Tadic', J., Gore, W., Bui, T. P., Dean-Day, J. M., and Chang, C. S.: Quantification of CO2 and CH4 emissions over Sacramento, California, based on divergence theorem using aircraft measurements, Atmospheric Measurement Techniques, 12, 2949–2966,
- 730 https://doi.org/10.5194/amt-12-2949-2019, 2019.





- Turnbull, J. C., Karion, A., Fischer, M. L., Faloona, I., Guilderson, T., Lehman, S. J., Miller, B. R., Miller, J. B., Montzka, S., Sherwood, T., Saripalli, S., Sweeney, C., and Tans, P. P.: Assessment of fossil fuel carbon dioxide and other anthropogenic trace gas emissions from airborne measurements over Sacramento, California in spring 2009, Atmos. Chem. Phys., 11, 705–721, doi:10.5194/acp-11-705-2011, 2011.
- Watson, C. D., Wang, C., Lynar, T., and Weldemariam, K.: Investigating two super-resolution methods for downscaling 735 precipitation: ESRGAN and CAR, arXiv [preprint], https://doi.org/10.48550/ARXIV.2012.01233, 2020. Wu, Y., Teufel, B., Sushama, L., Belair, S., and Sun, L.: Deep Learning-Based Super-Resolution Climate Simulator-Framework 48, e2021GL094737, **Emulator** for Urban Heat Studies, Geophys. Res. Lett., https://doi.org/10.1029/2021GL094737, e 2021.
- Yong, H., Allen, G., Mcquilkin, J., Ricketts, H., Shaw, J.T.: Lessons learned from a UAV survey and methane emissions calculation at a UK landfill, *Waste Manag.*, 180 (47-54), https://doi.org/10.1016/j.wasman.2024.03.025, 2024.